



This is a repository copy of *Microstructure evolution of railway pearlitic wheel steels under rolling-sliding contact loading*.

White Rose Research Online URL for this paper:
<https://eprints.whiterose.ac.uk/166455/>

Version: Accepted Version

Article:

Hu, Y., Zhou, L., Ding, H.H. et al. (4 more authors) (2021) Microstructure evolution of railway pearlitic wheel steels under rolling-sliding contact loading. *Tribology International*, 154. 106685. ISSN 0301-679X

<https://doi.org/10.1016/j.triboint.2020.106685>

Article available under the terms of the CC-BY-NC-ND licence
(<https://creativecommons.org/licenses/by-nc-nd/4.0/>).

Reuse

This article is distributed under the terms of the Creative Commons Attribution-NonCommercial-NoDerivs (CC BY-NC-ND) licence. This licence only allows you to download this work and share it with others as long as you credit the authors, but you can't change the article in any way or use it commercially. More information and the full terms of the licence here: <https://creativecommons.org/licenses/>

Takedown

If you consider content in White Rose Research Online to be in breach of UK law, please notify us by emailing eprints@whiterose.ac.uk including the URL of the record and the reason for the withdrawal request.



eprints@whiterose.ac.uk
<https://eprints.whiterose.ac.uk/>

Microstructure evolution of railway pearlitic wheel steels under rolling-sliding contact loading

Y. Hu^{a,b}, L. Zhou^a, H. H. Ding^a, R. Lewis^b, Q.Y. Liu^a, J. Guo^a, W.J. Wang^{a,*}

^a Tribology Research Institute, State Key Laboratory of Traction Power, Southwest Jiaotong University,

Chengdu 610031, China

^b Department of Mechanical Engineering, the University of Sheffield, Mappin Street, Sheffield S1 3JD, UK

Abstract: The objective of this work is to investigate the microstructure evolution of railway pearlitic wheel materials (ER7, CL60 and C-class) under a rolling-sliding contact loading. Firstly, microstructures of CL60 wheel steel at different depths from the strain-free matrix to the top surface were systematically investigated via laser scanning confocal microscope (LSCM), scanning electron microscopy (SEM), electron backscattered diffraction (EBSD), transmission electron microscopy (TEM) and X-ray diffraction (XRD). Secondly, the differences in microstructures of the top layers of those three types of wheel steels were explored. At last, the correlation between microstructure evolutions and their wear and rolling contact fatigue (RCF) behaviours was discussed. These information could provide a guide in development of premium railway wheel materials and choosing wheel materials.

Keywords: Microstructure evolution; Continuous dynamic recrystallization; TEM analysis; Grain refinement

1. Introduction

Repair and replacement of railway wheels, due to the severe wear or rolling contact fatigue

* Corresponding author. Tel: +86-28-87634304.

E-mail address: wwj527@swjtu.cn (W.J. Wang).

(RCF) damage, have always been a major proportion of Chinese high-speed railway operating cost [1]. Developing premium wheel materials with improved tribology properties have been considered to be an effective way to prevent such degradations. Wheels with different microstructures, such as bainitic wheels [2], laser cladding wheels [3], spheroidized pearlite wheels [4], etc., have been widely developed. However, the traditional lamellar pearlitic wheel steels are still commonly used in railways in various countries because of their excellent wear and RCF resistance and superior work-hardening ability. In recent years, premium pearlitic wheel materials possessing excellent mechanical properties have been developed through increasing the carbon content and refining the lamellar structure via alloying or heat treatment [5]. In order to explore the effect of wheel hardness on wear regimes and RCF damage evolution, a series of small-scale experiments were carried out on three standard pearlitic wheel materials (ER7, CL60 and C-class) currently used in the high-speed railways in China (see reference [6] for more details). It is worth noting that different pearlitic wheel steels possess different microstructures. Therefore, in addition to understanding the effect of wheel hardness on the wear response, a systematic investigation on the microstructure evolutions of wheel materials should be carried out.

With the application of advanced material analysis methods (scanning electron microscopy (SEM), electron backscattered diffraction (EBSD), transmission electron microscopy (TEM), X-ray diffraction (XRD), etc.), it was found that the microstructures of the wheel and rail materials were changed significantly during operation. He *et al.* [7] found that a gradient structure appeared in the depth direction of a pearlite wheel material. EBSD measurement indicated that the wheel and rail materials experienced the strain-induced grain refinement

under cyclic loading [8]. With the accumulation of strain, the wheel and rail surface layers were significantly deformed and refined to form a nano-crystalline structure with high-angle grain boundaries (HAGBs).

The evolution of microstructure caused significant changes in the mechanical properties which will further affect the wear resistance and fatigue crack propagation of wheel and rail materials. Pan *et al.* [9] found that the microstructure of the wheel surface varied at different wear stages, and the CL65 wheel steel presented the best wear resistance when the outermost layer was sub-grain structure. Different microstructures were observed at the crest and trough of the D2 pearlitic wheel material which underwent polygonisation wear, and the troughs exhibited more significant work-hardening and grain refinement [10]. A martensite white etching layer (WEL) with high hardness and low fracture toughness was formed on the contact surface, which could accelerate the development of radial cracks [11]. Notably, the EBSD analysis around the crack path of rail steels showed that the crystal orientation and grain boundary distribution had significant effects on fatigue crack initiation and propagation. Masoumi *et al.* found that grains orientated along the train passage plane were highly prone to crack propagation [12].

In summary, the wear and RCF crack growth mechanisms of wheel materials are closely related to the microstructure evolution (such as grain size changing, crystal orientation changing and dislocation movement) during the plastic deformation. However, the influences of microstructure evolutions of pearlitic wheel materials with various hardness values on their wear and RCF behaviors have not yet been explored systematically. Therefore, this study aimed to systematically investigate the microstructure evolutions of ER7, CL60 and C-class wheel

materials, and further explore the correlation between the microstructure evolution and their wear and RCF mechanisms [6] at the micro scale.

2. Experimental procedure

2.1 Materials and experimental parameters

Three types of pearlitic wheel materials, ER7, CL60 and C-class, were explored in this study. Wheel and rail samples were cut from the treads of ER7, CL60 and C-class wheels and the head of U75V rail. Their chemical compositions and hardness values are exhibited in Table 1. The hardness values of ER7, CL60 and C-class wheel steels are 296 HV_{0.5}, 327 HV_{0.5} and 388 HV_{0.5}, respectively. The carbon contents of these wheel materials show an ascending trend with their hardness values, which are ≤ 0.48 wt%, 0.55 ~ 0.65 wt% and 0.67 ~ 0.77 wt%, respectively. The microstructures of wheel and rail materials are presented in Fig. 1. All these wheel materials have the ferrite-pearlite microstructure (i.e., proeutectoid ferrite and lamellar pearlite). Pearlite colonies consist of alternating ferrite and cementite lamellae. The proeutectoid ferrite contents of ER7, CL60 and C-class steels decrease with the increase in the hardness (Fig. 1a-c). The circular line method was used to measure the average pearlite lamellar spacing (Sp) [13]. $Sp=0.5L/N$, where L is the length of circle and N is the number of intersections between the circular and the lamellae. The statistical results show a declining trend in the Sp values of ER7, CL60 and C-class wheel materials, which are 126.1±32 nm, 104.7±21 nm and 96.8±28 nm, respectively.

The rolling-sliding experiments were performed on a twin-disc testing rig (WR-1, China), which allowed two discs to run against each other with normal and tangential forces to simulate

the rolling-sliding contact between wheel and rail. The diameter was 40 mm for the wheel and rail discs, and the contact width between the two discs was 5 mm. The contact pressure was set at 850 MPa, which simulated the general contact pressure on the standard worn tread of wheels in China [14]. All tests were performed for 1.8×10^5 cycles with a creepage of 0.91% and a rotational speed of 200 r/min [6].

2.2 Microstructural analysis methods

The cross sections of wheel samples were cut along the rolling direction after experiments [6], and prepared for LSCM (VK-9700, Japan) and SEM (JSM-7800FPRIME, Japan) observations by standard metallographic procedures. The hardness as a function of the depth was measured using a Vickers hardness instrument (MVK-H21, Japan) with the load of 0.49 N ($HV_{0.05}$) for 10 s dwell time.

The phase constitutions of CL60 wheel material were detected at different depths via XRD (Empyrean, Netherlands) with a Cu-K α radiation. Phase analyses were performed in a 2θ -range between 35° and 85° with 0.02 2θ step size. The test sample was a 10 mm*10 mm cross section cut along the rolling direction. After polishing, it was marked with the hardness instrument along the depth direction, and finally a micro-area XRD test was performed at a distance of about 30 μm and 1 mm from the contact surface.

The EBSD samples were taken from various depths of wheel samples. Those samples were first ground with a 1200-grit SiC paper and then electro-polished in a solution containing 12 ml distilled water, 80 ml alcohol and 8 ml perchloric acid at a voltage of 16 V for 20 ~ 30 seconds. EBSD analysis was performed on a Hitachi S-3400N SEM equipped with an HKL-EBSD

system with the accelerating voltage of 20 kV, the emission current of 80 μ A, the working distance of 14 ~ 17 mm, and the specimen tilt-angle of 70°. The step size of the scans was defined as 0.15 μ m or 0.3 μ m depending on the size of the scanned areas.

Furthermore, the dislocations and crystallization evolution of wheel samples after the rolling-sliding wear tests were observed using a Hitachi H-800 TEM, working with the selected-area electron diffraction (SAED), conventional bright-field (BF) and dark-field (DF). Samples for TEM observation were prepared as follows: firstly, a thin slide was cut with a thickness of about 2 mm from the worn trace of wheel materials through a wire cutting machine, then the slide was thinned to about 50 ~ 80 μ m through mechanical grinding, and then the slide was further thinned to a standard thickness of \leq 500 nm via the electrolytic double spray in a solution containing 5 ml perchloric acid and 95 ml alcohol at a voltage of 80 V.

3. Results

3.1 Microstructure evolution with depth

3.1.1 LSCM, SEM and EBSD observations

Fig. 2 presents the microstructure evolution of CL60 wheel steel after the rolling-sliding test. Various sections at different depths from the contact surface were observed using LSCM for the overall morphology (Fig. 2a), SEM for the evolution of lamellar pearlite (Fig. 2b,e,h) and EBSD for changes of ferrite grains and their orientations (Fig. 2c,d,f,g,i,j). Inverse Pole Figures (IPF) in colours (Fig. 2c,f,i) visualize the structure of ferrite lattice domains. Grain boundary plots (Fig. 2d,g,j) can reveal the grain boundary angle and grain size. The green curves represent low-angle grain boundaries (LAGBs) of $< 15^\circ$ and black curves represent high-angle

grain boundaries (HAGBs) of $15^\circ \sim 65^\circ$. Fig. 2 shows that under the rolling-sliding loading, the wheel surface layer underwent significant plastic deformation. According to the deformation extent, the wheel surface layer could be divided into three zones: severe plastic deformation (SPD) zone ($0 \sim 50 \mu\text{m}$ below the surface), transition zone ($50 \sim 200 \mu\text{m}$ below the surface) and matrix material, as shown in Fig. 2a. The microstructure evolution in depth (i.e., the differences in these three zones) can reflect the process of plastic deformation and defect accumulation in the wheel materials during rolling-sliding conditions.

The strain-free matrix material of CL60 material presents a nearly perfect lamellar structure with a random distribution of the lamellar orientation (Fig. 2h). Neither the distortion nor the local misorientation (Fig. 2i,j) is significant in the matrix material which possesses an average grain diameter of about $10.7 \mu\text{m}$.

In the early stage of deformation (i.e., transition zone), pearlite colonies are compressed by the normal force and stretched in the shear stress direction. The original lamellar cementite starts to bend, fragment and break into granules and the “net-like” ferrite flows in the deformation direction, as shown in Fig. 2e. Meanwhile, the grain size reduces rapidly in the transition zone, forming a sub-grain structure with an average grain diameter of $1.19 \mu\text{m}$ (Fig. 2g). The $\{101\}$ oriented grains with green colour in Fig. 2f are dominant in the rolling direction (RD) plane due to the slippage and deflection of ferrite grains in the direction of shear stress.

In the SPD zone, the pearlite colonies are severely fragmented and rearranged to form a fibrous structure parallel to the surface (Fig. 2b). The grains are further refined to form an ultra-fine grain structure with an average grain diameter of $0.87 \mu\text{m}$. Meanwhile, the grains are randomly oriented in the SPD zone (Fig. 2c).

Besides, with an increase in plastic deformation, the fraction of HAGBs increases obviously with a simultaneous refinement of grains, from 48.57% in the transition zone (Fig. 2g) to 67.13% in the SPD zone (Fig. 2d). This structural change indicates that the wheel steel underwent dynamic recrystallization. Conventionally, the dynamic recrystallization, which is now referred as to discontinuous dynamic recrystallization (dDRX), is characterized by a nucleation and growth process and takes place at high enough temperatures (450~650°C for hypoeutectoid steels). However, under the cyclic rolling-sliding contact loading in the present work, the dynamic recrystallization can be completed at a lower temperature (the previous work on temperature showed that the temperature was below 100 °C at the wheel/rail contact under the 1500 MPa pressure and 1% creepage [15]) due to severe deformation. This phenomenon has been referred as to continuous dynamic recrystallization, i.e., cDRX [16].

Fig. 3 presents the distributions of the grain boundary misorientation in the transition zone and SPD zone. “Correlated” and “Random” imply misorientation calculated using neighboring points for the target material and a purely random texture, respectively [17]. For the “correlated” grain boundaries, a misorientation angle around 2° occupies the largest fraction in the transition zone (Fig. 3a), while this fraction decreases dramatically in the SPD zone (Fig. 3b). The average “correlated” misorientation angle in the transition zone is smaller than that in the SPD zone. This implies once again that during the accumulation of plastic deformation, the wheel surface layer has undergone a transformation from sub-grains with LAGBs to ultra-fine grains with HAGBs.

Fig. 4 shows the pole figures (PFs) in the transition zone and SPD zone. The PF is the polar density distribution obtained by the stereographic projection of the crystal on a certain

crystal plane. It is commonly used to analyze texture, i.e., the high polar density represents the preferred orientation of the crystal. The maximum intensity of the transition zone in the PF is 5.06, which is higher than the maximum intensity of the SPD zone (3.83). This also suggests that the microstructure of the transition zone has preferential orientation features due to the sliding of the grains in the direction of shear stress. With the increase in deformation, this preferred orientation gradually weakens. Although the faint shear deformed texture in the {110} plane can be seen in Fig. 4b, the reducing polar density in the SPD zone supports the occurrence of cDRX in Fig. 2c,d.

The evolution of geometrically necessary dislocation densities (ρ^{GND}) with deformation could further confirm the existence of cDRX process. The Local Misorientation (LocMis), which is positively correlated with ρ^{GND} , is given in Fig. 5. Clearly, the LocMis in the transition zone is higher than that in SPD zone (Fig. 5c), indicating a substantial declining of ρ^{GND} with the reducing depth from worn surface. The shear deformed texture generally has a high ρ^{GND} . Accordingly, the transition zone presents a shear deformed texture (Fig. 2f and g, Fig. 4a), with further deformation, the structure changes to well recrystallized microstructures in SPD zone (Fig. 2c and d, Fig. 4b).

3.1.2 TEM observations

In order to further study the dislocation movements and cDRX process of wheel materials during rolling-sliding loading, the micro-morphologies and the selected-area electron diffraction (SAED) observations for different zones of CL60 wheel steel were performed using TEM, as seen in Fig. 6. Since the microstructure in the top surface was severely deformed and the pearlite features were hardly visible, TEM observation of the SPD zone was taken at the

depth of about 40 μm from the surface (Fig. 6a-c). The transition zone (Fig. 6d-f) and the matrix material (Fig. 6g-i) were observed at the depth of 110 μm and 1 mm from the surface, respectively.

Obviously, the dislocation density is relatively low in the matrix CL60 wheel steel (Fig. 6g-i). A few random dislocations are visible in the proeutectoid ferrite in Fig. 6i.

In the transition zone, shear bands (Fig. 6d,e) are generated in the lamellar pearlitic, and the mutually crossed shear bands further subdivide the original lamellar pearlitic into multiple fine grains under the normal and tangential forces. It is well known that the dislocation density in materials increases with the extent of plastic deformation [18]. The formation of shear bands is caused by the slip and intersection of dislocations in regions with high dislocation density [19]. Meanwhile, a sub-grain structure with a grain size of 1 ~ 3 μm is formed in the ferrite phase (Fig. 6f). The LAGBs in this structure result from the spontaneous movement of dislocations to the low-energy state under the rolling-sliding loading [16].

In the SPD zone, pearlite colonies are severely broken into ultra-fine grains with a size of about 400 nm under the action of shear bands (Fig. 6b). Meanwhile, the sub-grains in ferrites transform to nano-grains with HAGBs (Fig. 6c). Besides, the SAED pattern changes from single crystal lattice in matrix material (inset images in Fig. 6h) to polycrystalline rings (inset image in Fig. 6a), which also implies the grain refinement.

3.1.3 XRD observations

Micro-area XRD analysis was performed on the SPD zone and the matrix material of CL60 wheel to investigate the phase changes, as shown in Fig. 7. Compared with the matrix material, the intensities of the (110) α , (200) α and (211) α peaks in the SPD zone are significantly

weakened. Meanwhile, those three peaks in the SPD zone are broadened. The full width at half maximum (FWHM) is broadened by 153% at $(110)\alpha$, 94% at $(200)\alpha$ and 85% at $(211)\alpha$. The broadening of the ferrite phase peaks suggests that micro-strain and grain refinement occur in the SPD zone of CL60 wheel.

3.2 Microstructure evolutions of three types of pearlitic wheel steels

3.2.1 SEM observations

Fig. 8 presents SEM images of SPD zones and transition zones for ER7 and C-class wheel materials. These two wheel steels also underwent the cDRX process as CL60 (Section 3.1). However, some differences among the three wheel steels are visible because of their different matrix microstructures. The C-class wheel steel is dominated by lamellar pearlite fragmentation due to its extremely low ferrite content (Fig. 8c,d), while ER7 and CL60 steels possess slender ferrite flow lines (Fig. 8a,b and Fig. 8b,e) in addition to pearlite fragmentation.

3.2.2 TEM observations

Fig. 9 shows the TEM images of ER7 wheel steel in the SPD zone. For the ER7 steel with the highest ferrite content and the lowest hardness, the LAGBs sub-grains in ferrite and lamellar pearlite features can still be seen in the SPD zone at 40 μm from the surface. These sub-grains are non-equiaxed, with a major axis of about 1 μm and a minor axis of about 500 nm.

However, for the CL60 wheel material which possesses the lower ferrite content and the higher hardness, the ferrite has been completely recrystallized at the depth of 40 μm from the surface, and the pearlite has been severely broken, forming an ultra-fine crystal structure with HAGBs in the SPD zone (Fig. 6a-c). Therefore, at the same depth (40 μm from the surface) in the SPD zone, the difference between the crystal structures of ER7 and CL60 steels is that: the

ER7 wheel is dominated by non-equiaxed sub-grains with a major axis of about 1 μm (Fig. 9), and the CL60 wheel is typified by equiaxed ultra-fine grains with a size of about 400 nm (Fig. 6a-c).

Fig. 10 shows TEM images in the SPD zone, transition zone and the matrix material of C-class wheel steel. The un-deformed C-class steel has random ferrite/cementite lamellae arrangements and contains proeutectoid ferrites in small quantities (Fig. 10g,h). Because of the smallest S_p of the C-class steel, cementite diffraction spots can be found in the ferrite SAED pattern of the [001] zone axis (Fig. 10i).

With the development of plastic deformation, the proeutectoid ferrite changes from sub-grains induced by dislocation movement in the transition zone (Fig. 10d) into the equiaxed ultra-fine grains with HAGBs in the SPD zone (Fig. 10a) in the C-class wheel. This process is the same as the cDRX of CL60 steel (Section 3.1). Interestingly, the cross arrangement of the lamellar pearlite caused by severe extrusion can be found in the transition zone (Fig. 10e) in C-class wheel. Meanwhile, a double-layer structure (i.e., a new layer of lamellar pearlite structure arranged upon the original layer at an angle with the original lamellae orientation, forming crossed shear bands) is observed in the transition zone of C-class steel (Fig. 10f).

In the SPD zone with a depth of 40 μm from surface, the grains are so fine that the lamellar structure is not visible, and even the individual grains are hard to be found (Fig. 10a-c). In Fig. 10a, the (211) Fe_3C and (200) Fe_3C rings can be seen in the SAED pattern with polycrystalline rings. Besides, a lamellar block structure appears in this zone, as shown in Fig. 10c.

Compared with ER7 and CL60 wheel steels, at the same depth (40 μm from surface) in the SPD zone, the high-hardness C-class wheel has an ultra-fine grain structure with the

smallest grain size (hardly measured using TEM).

4. Discussion

4.1 Strain-induced microstructure evolution

The mechanism of microstructure evolution in this work is the same as seen in a previous study [7]. The microstructural evolution process of the wheel material was divided into four stages: the initial plastic deformation and dislocation accumulation, the formation of dense dislocation walls (DDWs) and dislocation tangles (DTs), the transition of DDWs and DTs into sub-boundaries, and the formation of nanocrystalline grain structures. Due to the continuous deformation, it is hard to separate the initial stage of deformation and dislocation accumulation from the formation of DDWs and DTS. Therefore, the cDRX process was divided into three stages in this work, similar to the previous study [20]. According to the evolution of cementite lamellae structure, dislocation movement and grain boundaries with depth from the surface (Section 3.1 and Section 3.2), a schematic illustration of microstructure evolution with increasing strain was plotted, as shown in Fig. 11a,b.

The stage I was accomplished with the formation of DDWs and DTs in ferrite and pearlite phases through propagation, slip, annihilation and recombination of the dislocations (Fig. 11a). Meanwhile, accompanied by the plastic flow, compression and thinning were observed for colonies oriented parallel to the shear plane, whilst bending and breaking were observed perpendicular to the shear plane (Fig. 2e, Fig. 8b and Fig. 11b). In this stage, the lamellar structure of pearlite steel can still be observed via SEM.

The further increase in strain (stage II) resulted in the transformation of DDWs and DTs

into sub-grains with LAGBs in ferrites and shear bands in pearlites (Fig. 2f,g, Fig. 6d-f, Fig. 9, Fig. 10d-f and Fig. 11a). Meanwhile, dense dislocation tangles and pile-ups could still be observed in the refined ferrite and pearlite sub-grains (Fig. 6d-f, Fig. 9 and Fig. 10d-f). This was accompanied by further thinning, bending and fragmenting of cementite lamellae and appearance of fibrous structure, as shown in Fig. 8d.

As deformation proceeded (stage III), the rearrangement and annihilation of dislocations in sub-grains led to the formation of equiaxed ultra-fine grains with an average grain diameter of 0.87 μm (Fig. 2c,d, Fig. 6a-c, Fig. 10a-c and Fig. 11a). Besides, the fraction of HAGBs was increased from 48.57% to 67.13% (Fig. 2d and Fig. 3). With the completion of cDRX, a uniform fibrous structure was formed in the SPD zone, and the lamellar feature could not be observed by SEM (Fig. 2b and Fig. 8a,c).

4.2 Strain-induced work-hardening

In the present work, the contact pressure and the friction coefficient were known to cause a shear stress (τ_{xz}) which exceeded the shear yield strength of the three wheel materials (k). Therefore, the plastic flow and residual stresses were generated and accumulated in the surface layer during cyclic loading. The plastic flow raised the wheel elastic limit, while residual stresses suppressed the plastic flow. This combined effect is described as “shakedown” or “strain hardening” [21]. The shear yield strength k_0 (black dotted line in Fig. 11d) of the wheel material is constant in the matrix material. The subsurface material could be divided into two regions depending on the distribution of the shear stress (τ_{xz}): stable area ($\tau_{xz} < k_0$, below point S) and hardened area ($\tau_{xz} \geq k_0$, above point S) [22].

Similarly to the microstructural evolution in depth, there were also three stages of the

increase in the hardness, as shown in Fig. 11c,d. In the stage I (depth > 150 μm) with slight plastic flow, the hardness value remained practically at a stable level (see Fig. 11c). It has been reported that during severe deformation, the refinement of ferrite grains could lead to an increase in shear yield strength of the material [23]. In the stage II (50 μm < depth < 150 μm) with obvious plastic flow, the shear yield strength of the deformed material was enhanced from k_0 to k_t (red dotted curve in Fig. 11d) and the material was rapidly hardened (Fig. 11c). In the stage III (depth < 50 μm) with severe plastic deformation, the enhanced shear yield strength k_s (blue dotted curve in Fig. 11d) reached the maximum value and the hardness slowly increased to a maximum value of 665 HV_{0.05} (Fig. 11c). This decreasing hardening rate is related to the evolution of strain rate, and it was reported that there was an asymptotic relationship between strain rate and contact cycles, which means that the strain rate gradually decreased to reach near saturation [24].

4.3 Differences in microstructure evolutions among three pearlitic wheel steels

The microstructures of three pearlitic wheel steels can be compared, as shown in Table 2. Under the same rolling-sliding contact loading (850 MPa contact pressure, 0.91% creepage), all three pearlitic wheel steels underwent the cDRX process as mentioned in Section 4.1. Their microstructures were shifted from the lamellar structure to the fibrous structure, and the grains were refined with the plastic deformation.

Because of the low carbon content and the high proeutectoid ferrite content in the matrix material of ER7 and CL60 (Fig. 1a, b), dense ferrite flow lines, thinning and fragmentation of pearlite lamellae were observed (Fig. 8a and Fig. 2b) in the SPD zone (40 μm from surface). Whereas, ferrite flow lines can be hardly observed in the fibrous structure of C-class steel (Fig.

8c), which possesses the less proeutectoid ferrite in the matrix material (Fig. 1c).

Meanwhile, for the refined structures in SPD zones, the ER7 was dominated by non-equiaxed sub-grains of about 1 μm length and with LAGBs (Fig. 9); the CL60 had completed the cDRX process, forming equiaxed ultra-fine grains of about 400 nm diameter and with HAGBs (Fig. 2d, Fig. 6a-c); the C-class steel had a nano-crystalline structure with HAGBs (Fig. 2d, Fig. 6a-c), and it was hard to measure the grain size by TEM. In summary, at the same depth from surface, C-class with the lowest ferrite content presented the highest cDRX degree, followed by the CL60 and ER7steels.

4.4 Correlation between microstructure evolutions and wear and RCF behaviours

Based on the above results in microstructures and the data of wear and fatigue cracks obtained in Reference [6], the correlation between microstructure evolutions and wear and RCF behaviors can be explored.

During the cyclic loading, the plastic flow and strain hardening of wheel materials in Section 4.1 could be accumulated up to failure. This process is described as “ratcheting” [21]. Ratchetting can lead to the generation of fatigue cracks and even RCF failure, and when the thin flakes of material was detached, it also caused wear [25].

Table 2 shows that the wear rates and average fatigue crack lengths of ER7, CL60 and C-class pearlitic steels gradually decreased. An important reason was that the harder wheel material possessed a higher shear yield strength k ($k_{ER7} < k_{CL60} < k_{C-class}$ at the same depth), thereby had a greater stable area, as shown in Fig. 12a (point $S_{C-class}$ was above the points S_{CL60} and S_{ER7}). Meanwhile, the post-test surface hardness of ER7, CL60 and C-class pearlitic steels gradually increased (Fig. 12b), further leading to a gradual increase in their wear resistances.

The increment of hardness between the matrix and sub-surface, as shown in Fig. 12b, is from a combination of microstructure-induced hardening and strain-induced work hardening. In a study [26] of RCF tests for untreated and laser shock peening (LSP) treated ER8 wheel, it was found that the magnitude of strain hardening of untreated wheel steel with lower matrix hardness was larger than LSP-treated steels. The LSP usually does not change the microstructure of the wheel material, so this result means that the magnitude of strain-induced hardening decreased with the increasing matrix hardness for the same wheel material. Therefore, the biggest hardness increment occurring on C-class steel may mainly result from the microstructure evolution, rather than the rolling contact strain. This speculation can be supported by the reduction in the recrystallized grain sizes of ER7, CL60 and C-class steels in the SPD zone (Table 2).

The differences in microstructure evolutions among those three types of wheel steels was also an important factor that affected the wear and RCF resistance. Fig. 13 presents the surface damages and RCF cracks of ER7 and C-class wheel steels. The main wear mechanism of the three pearlitic wheel steels was fatigue wear. The surface damage was mainly peeling, while the C-class steel with the lowest ferrite content presented the slightest peeling (Fig. 13b). Meanwhile, the fatigue crack morphologies of the three pearlitic materials were different. Specifically, ER7 and CL60 wheel steels were dominated by slender surface cracks and subsurface cracks with openings (Fig. 13c), and the average crack lengths were 333 ± 98 μm and 207 ± 101 μm , respectively (Table 2). Whereas, the C-class steel was typified by short cracks with an average length of 71 ± 32 μm , and the cracks contained broken materials inside the interlayer (Fig. 13d).

The main reason for the difference in RCF damage is the different proeutectoid ferrite contents among the wheel steels. It was reported that the micro-cracks initiation preferentially occurred in ferrite and grew along the highly strained ferrite pathways, since the ductility exhaustion in the ferrite began earlier than pearlite due to the earlier plastic deformation and higher increase rate in the ferrite [27]. Therefore, for ER7 and CL60 wheel steels with high ferrite contents, cavities which were generated via dislocation annihilation [28] grew and joined to form micro-cracks in strained ferrite. With the further propagation of micro-cracks along the dense ferrite flow lines, the slender fatigue cracks with openings appeared in ER7 and CL60 wheel steels. Furthermore, such cracks propagated to the contact surface and appeared as flakes peeling away (Fig. 13a). The fracture and detachment of material from the surface caused the formation of wear debris, resulting in a high wear rate of ER7 and CL60 steels (Table 2).

Whereas, concerning the C-class wheel with the low ferrite content, crack initiation along strained ferrite was still present, but not so dominant, and there were no ferrite flow lines to provide a route for cracks to join and propagate, therefore, the cracks were relatively short. In addition, at the same depth from surface, the C-class pearlite steel had the finest structure (Table 2). The dense HAGBs and ferrite/cementite interfaces in the top layer of C-class steel could hinder its plastic flow and crack propagation, resulting in the generation of short cracks with interlayers of broken materials (Fig. 13d). Furthermore, the peeling on the C-class wheel surface was mild (Fig. 13b). Therefore, the wear resistance and anti-RCF property of C-class material was significantly better than ER7 and CL60 wheel materials.

5. Conclusions

The microstructure evolutions of three types of railway pearlitic wheel materials (ER7, CL60 and C-class) with different ferrite contents were systematically studied via LSCM, SEM, EBSD, TEM and XRD. The correlation between microstructure evolution and the wear and RCF behaviours was explored. The following conclusions can be drawn:

1. During the cyclic rolling-sliding contact loading, the three wheel materials (ER7, CL60 and C-class) underwent strain-induced cDRX. At the low strain, DDWs and DTs in ferrite and pearlite phases were formed through propagation, slip, annihilation and recombination of the dislocations. The increase in strain resulted in a transformation of dense dislocation tangles and pile-ups into sub-grains with LAGBs in ferrites and shear bands in pearlites. Finally, ultra-fine grains with HAGBs were generated.
2. All those three pearlitic wheel steels presented a fibrous structure without the lamellar feature on the surface layer. Dense ferrite flow lines could be observed in the fibrous structure of ER7 and CL60 wheel steels, while no ferrite lines were visible in the C-class steel. With the decrease in ferrite content (i.e., from ER7, to CL60, and to C-class wheel), the cDRX degree was increased. Specifically, the grain size of ER7, CL60 and C-class steels was gradually decreased at depth of 40 μm depth from surface.
3. The deformation of ER7 and CL60 wheel steels with the high ferrite content was typified by ferrite flow and pearlite fragmentation. The dense plastic flow lines contributed to the propagation and joint of fatigue cracks, leading to the generation of slender cracks with openings, which further caused the high wear rates and severe RCF damages. The deformation of C-class material was dominated by pearlite fragmentation due to its low ferrite content. The finer nanocrystal structure with dense HAGBs in the deformed surface

layer hindered the plastic flow and crack propagation, and caused the improved wear resistance and anti-RCF properties.

4. The understanding on the correlation between the microstructure evolutions and the wear and RCF behaviors could provide theoretical support for the development of premium railway wheel materials. Evidences showed that the pearlitic wheel steel with the low ferrite content and high grain refinement ability during the plastic deformation could possess the excellent wear and damage resistances.

Conflicts of interest

There is no conflict to declare.

Author contributions

Y. Hu, H.H. Ding and W.J. Wang conceived and designed the experiments. Y. Hu and L. Zhou performed the sample preparation, carried out the experiments and materials characterization. R. Lewis, J. Guo, Q.Y. Liu, and Y. Hu analyzed the results. H.H. Ding and Y. Hu prepared the manuscript. All authors discussed the experimental results and commented on the manuscript. All authors read and approved the final manuscript.

Acknowledgements

The work was supported by National Natural Science Foundation of China (No. 51975489), Autonomous Research Project of State Key Laboratory (No.2020TPL-T10) China Postdoctoral Science Foundation (No. 2019M663548), Doctoral Innovation Fund Program of

Southwest Jiaotong University (No. D-CX201810) and Cultivation Program for the Excellent Doctoral Dissertation of Southwest Jiaotong University.

References

- [1] Y. Zhu, W.J. Wang, R. Lewis, W. Yan, S. Lewis, H.H Ding, A review on wear between railway wheels and rails under environmental conditions, *Journal of Tribology* 141(12) (2019).
- [2] A.B. Rezende, S.T. da Fonseca, F.M. Fernandes, R.S. Miranda, F.A.F. Grijalba, P.F.S. Farina, P.R. Mei, Wear behavior of bainitic and pearlitic microstructures from microalloyed railway wheel steel, *Wear* (2020) 203377.
- [3] W.J. Wang, R. Lewis, B. Yang, L.C. Guo, Q.Y. Liu, M.H. Zhu. Wear and damage transitions of wheel and rail materials under various contact conditions, *Wear* 362-363 (2016) 146-152.
- [4] G. Li, Z.Y. Hong, Q.Z. Yan, The influence of microstructure on the rolling contact fatigue of steel for high-speed-train wheel, *Wear* 342-343 (2015) 349-355.
- [5] P. Molyneux-Berry, C. Davis, A. Bevan, The influence of wheel/rail contact conditions on the microstructure and hardness of railway wheels, *The Scientific World Journal* (2014) 2014.
- [6] Y. Hu, L. Zhou, H.H. Ding, G.X. Tan, R. Lewis, Q.Y. Liu, J. Guo, W.J. Wang, Investigation on wear and rolling contact fatigue of wheel-rail materials under various wheel/rail hardness ratio and creepage conditions, *Tribology International* 143 (2020) 106091.
- [7] C.G. He, H.H. Ding, L.B. Shi, J. Guo, E. Meli, Q.Y. Liu, A. Rindi, Z.R. Zhou, W.J. Wang,

- On the microstructure evolution and nanocrystalline formation of pearlitic wheel material in a rolling-sliding contact, *Materials Characterization* 164 (2020) 110333
- [8] B. Dylewski, M. Risbet, S. Bouvier, The tridimensional gradient of microstructure in worn rails-Experimental characterization of plastic deformation accumulated by RCF, *Wear* 392 (2017) 50-59.
- [9] R. Pan, R.M. Ren, X.J. Zhao, C.H. Chen, Influence of microstructure evolution during the sliding wear of CL65 steel, *Wear* 400-401 (2018) 169-176.
- [10] J. Hua, X.J. Zhao, P.T. Liu, J.Z. Pan, C. Su, R.M. Ren, Study on the mechanism for polygonisation formation of D2 wheel steel and its effect on microstructure and properties under rolling wear conditions, *Wear* 450-451 (2020) 203261.
- [11] M. Messaadi, M. Steenbergen, Stratified surface layers on rails, *Wear* 414–415 (2018) 151–162.
- [12] M. Masoumi, E.A. Ariza, A. Sinatora, H. Goldenstein, Role of crystallographic orientation and grain boundaries in fatigue crack propagation in used pearlitic rail steel, *Materials Science and Engineering: A* 722 (2018) 147-155.
- [13] X. Hu, P. Van Houtte, M. Liebeherr, A. Walentek, M. Seefeldt, H. Vandekinderen, Modeling work hardening of pearlitic steels by phenomenological and Taylor-type micromechanical models, *Acta Materialia* 54 (2006) 1029-1040.
- [14] Z.Y. Yu, Research about the contact stress of wheel and rail, *Railway Locomotive & Car* 06 (2000) 1-9+4 (in Chinese).

- [15] W.T. Zhu, L.C. Guo, L.B. Shi, Z.B. Cai, Q.L. Li, Q.Y. Liu, W.J. Wang, Wear and damage transitions of two kinds of wheel materials in the rolling-sliding contact, *Wear* 398-399 (2018) 79-89.
- [16] T. Sakai, A. Belyakov, R. Kaibyshev, H. Miura, J.J. Jonas, Dynamic and post-dynamic recrystallization under hot, cold and severe plastic deformation conditions, *Progress in Materials Science* 60 (2014) 130-207.
- [17] Z.F. Yan, D.H. Wang, X.L. He, W.X. Wang, H.X. Zhang, P. Dong, C.H. Li, Y.L. Li, J. Zhou, Z. Liu, L.Y. Sun, Deformation behaviors and cyclic strength assessment of AZ31B magnesium alloy based on steady ratcheting effect, *Materials Science and Engineering: A* 723 (2018) 212-220.
- [18] X. Sauvage, W. Lefebvre, C. Genevois, S. Ohsaki, K. Hono, Complementary use of transmission electron microscopy and atom probe tomography for the investigation of steels nanostructured by severe plastic deformation, *Scripta Materialia* 60(12) (2009) 1056-1061.
- [19] T. Sakai, A. Belyakov, H. Miura, Ultrafine grain formation in ferritic stainless steel during severe plastic deformation, *Metallurgical and Materials Transactions A* 39(9) (2008) 2206.
- [20] Y. Ivanisenko, W. Lojkowski, R.Z. Valiev, H.J. Fecht, The mechanism of formation of nanostructure and dissolution of cementite in a pearlitic steel during high pressure torsion, *Acta Materialia* 51(18) (2003) 5555-5570.
- [21] A. Kapoor, Wear by plastic ratcheting, *Wear* 212(1) (1997) 119-130.
- [22] W.R. Tyfour, J.H. Beynon, A. Kapoor, The steady state wear behaviour of pearlitic rail steel under dry rolling-sliding contact conditions, *Wear* 180 (1995) 79-89.

- [23] T.R. Malow, C.C. Koch, Mechanical properties in tension of mechanically attrited nanocrystalline iron by the use of the miniaturized disk bend test, *Acta materialia* 46(18) (1998) 6459-6473.
- [24] X. Su, P. Clayton, Ratchetting strain experiments with a pearlitic steel under rolling-sliding contact, *Wear* 205 (1997) 137-143.
- [25] N.P. Suh, The delamination theory of wear, *Wear* 25(1) (1973) 111-124.
- [26] Y. Zhang, Q.L. Lian, X. Wang, Enhancement of rolling contact fatigue performance of ferrite-pearlite steel with laser shock peening, *Advances in Mechanical Engineering*, 11(5) (2019) 1-9.
- [27] J. Garnham, C. Davis, The role of deformed rail microstructure on rolling contact fatigue initiation, *Wear* 265 (2008) 1363-1372.
- [28] B. Hwang, S. Lee, Y.C. Kim, N.J. Kim, D.H. Shin, Microstructural development of adiabatic shear bands in ultra-fine-grained low-carbon steels fabricated by equal channel angular pressing, *Materials Science and Engineering: A* 441 (2006) 308-320.

Figure caption

Fig. 1: Microstructures of wheel and rail materials: (a) ER7 wheel; (b) CL60 wheel; (c) C-class wheel; (d) U75V rail.

Fig. 2: Microstructure evolution as a function of depth from the worn surface of CL60 wheel steel after the rolling-sliding experiment: (a) global view; (b-d) severe plastic deformation (SPD) zone taken from the topmost region; (e-g) transition zone at 110 μm below the surface; (h-j) matrix material at 1mm from the surface. RD means rolling direction and ND means normal force direction.

Fig. 3: Misorientation angle distributions in various regions: (a) transition zone; (b) SPD zone. “Correlated” and “Random” imply misorientation calculated using neighboring points for the target material and a purely random texture, respectively [17].

Fig. 4: Pole Figure (PF) in $\{001\}$, $\{111\}$ and $\{110\}$ crystal planes with an intensity legend: (a) transition zone; (b) SPD zone.

Fig. 5: Local Misorientation: (a) transition zone; (b) SPD zone; (c) data distribution.

Fig. 6: TEM images of CL60 wheel steel after the rolling-sliding experiment: (a-c) SPD zone, at a depth around 40 μm below the surface; (d-f) transition zone, with a distance of 110 μm from the surface; (g-i) matrix material taken from the un-deformed region, i.e., 1 mm below the surface.

Fig. 7: XRD patterns in the SPD zone and the matrix material of CL60 wheel steel.

Fig. 8: SEM images of ER7 and C-class wheel steels after the rolling-sliding experiment: (a) SPD zone and (b) transition zone of ER7 wheel; (c) SPD zone and (d) transition zone of C-class wheel. The SPD zones and the transition zones were taken at the topmost region and 110 μm

below the surface, respectively.

Fig. 9: TEM images of ER7 wheel steel in SPD zone (40 μm below the surface) after the rolling-sliding experiment.

Fig. 10: TEM images of C-class wheel steel after the rolling-sliding experiment, (a-c) SPD zone, at a depth around 40 μm from the surface; (d-f) transition zone, at the depth of 110 μm from the surface; (g-i) matrix material taken from the un-deformed region at 1 mm from the surface.

Fig. 11: Schematic illustration of cDRX and work-hardening: (a) process of cDRX [20]; (b) plastic deformation; (c) work-hardening; (d) mechanical analysis [22], where τ_{xz} is shear stress, k_0 is shear yield strength of the matrix material, k_t is shear yield strength of the transition zone material, k_s is shear yield strength of the SPD zone material.

Fig. 12: (a) Mechanical analysis [22], where k_{ER7} , k_{CL60} and $k_{C-class}$ mean material shear yield strengths of ER7, CL60 and C-class steels; (b) sub-surface hardness variation with depth from surface.

Fig. 13: Surface damages of (a) ER7 and (b) C-class wheels, and RCF cracks of (c) ER7 and (d) C-class wheels.

Fig. 1. Microstructures of wheel and rail materials: (a) ER7 wheel; (b) CL60 wheel; (c) C-class wheel; (d) U75V rail.

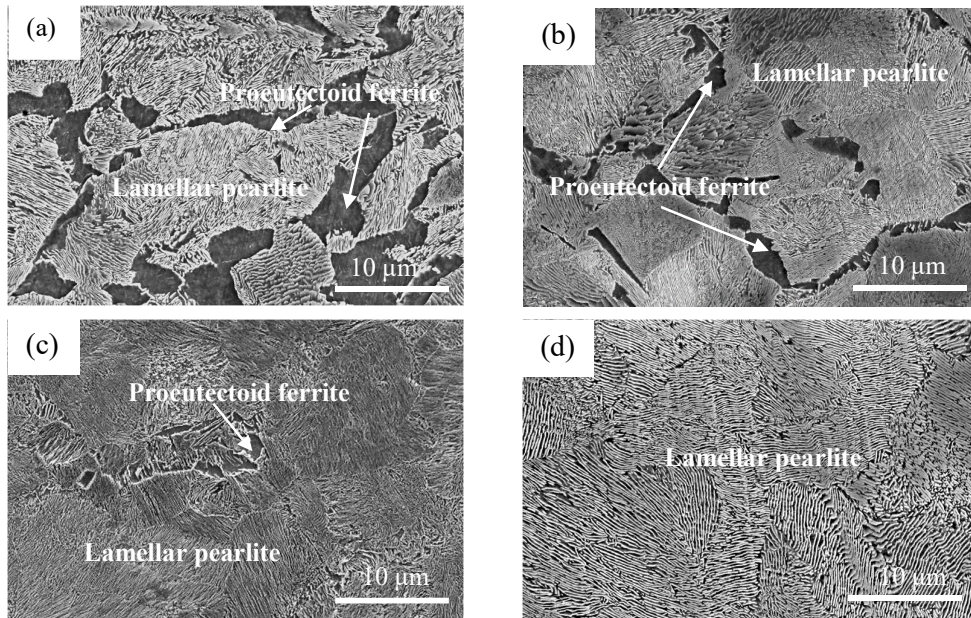


Fig. 2. Microstructure evolution as a function of depth from the worn surface of CL60 wheel steel after the rolling-sliding experiment: (a) global view; (b-d) severe plastic deformation (SPD) zone taken from the topmost region; (e-g) transition zone at 110 μm below the surface; (h-j) matrix material at 1 mm from the surface. RD means rolling direction and ND means normal force direction.

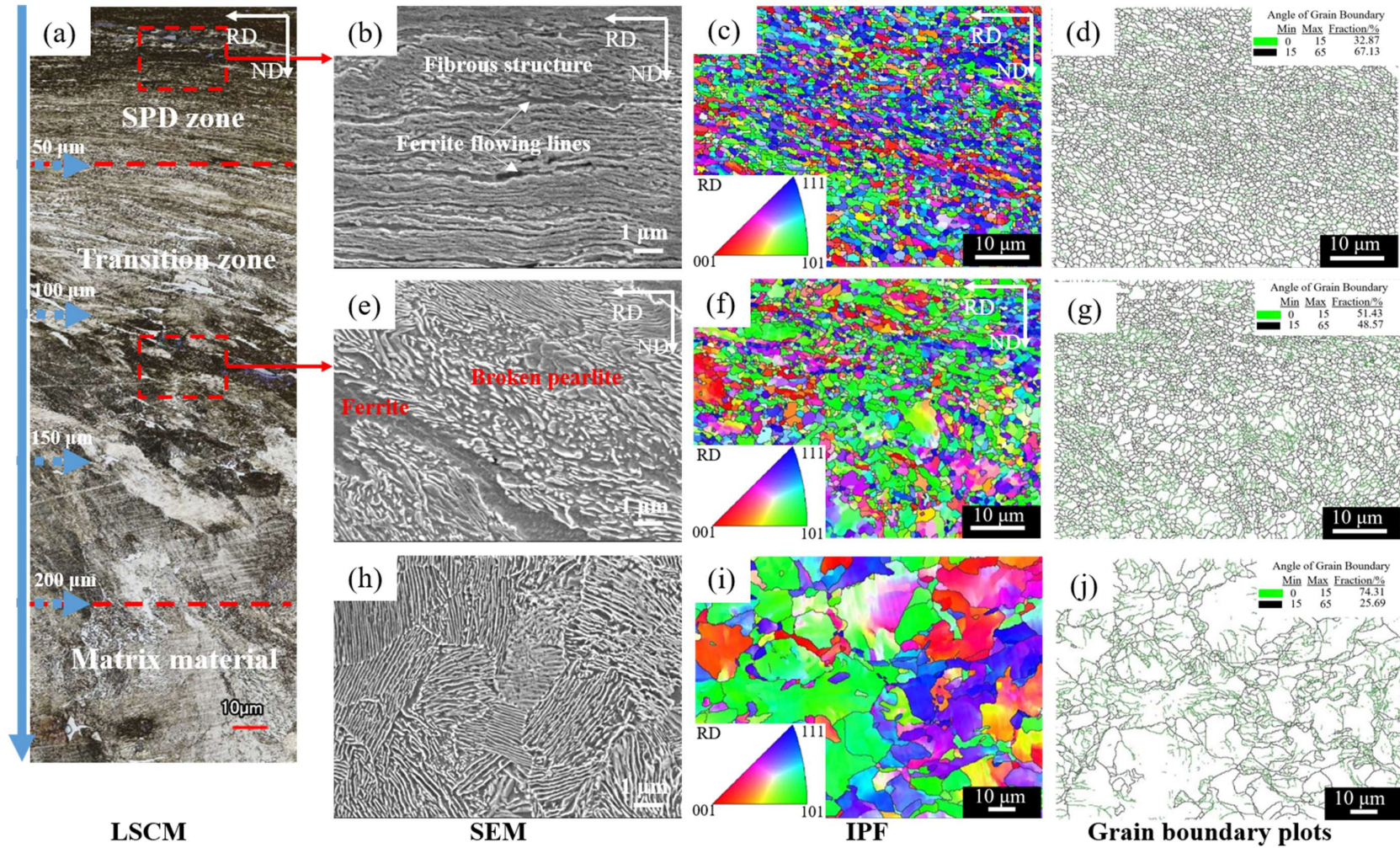


Fig. 3. Misorientation angle distributions in various regions: (a) transition zone; (b) SPD zone. “Correlated” and “Random” imply misorientation calculated using neighboring points for the target material and a purely random texture, respectively [17].

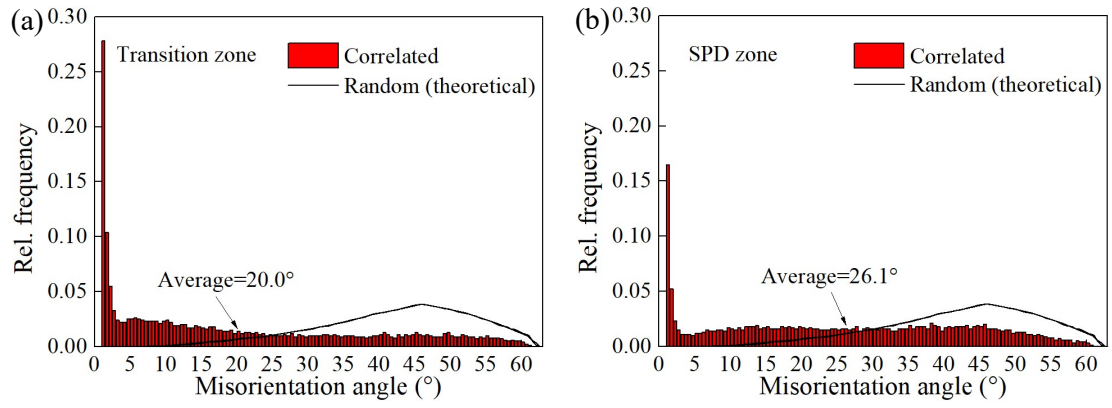


Fig. 4. Pole Figure (PF) in $\{001\}$, $\{111\}$ and $\{110\}$ crystal planes with an intensity legend: (a) transition zone;

(b) SPD zone.

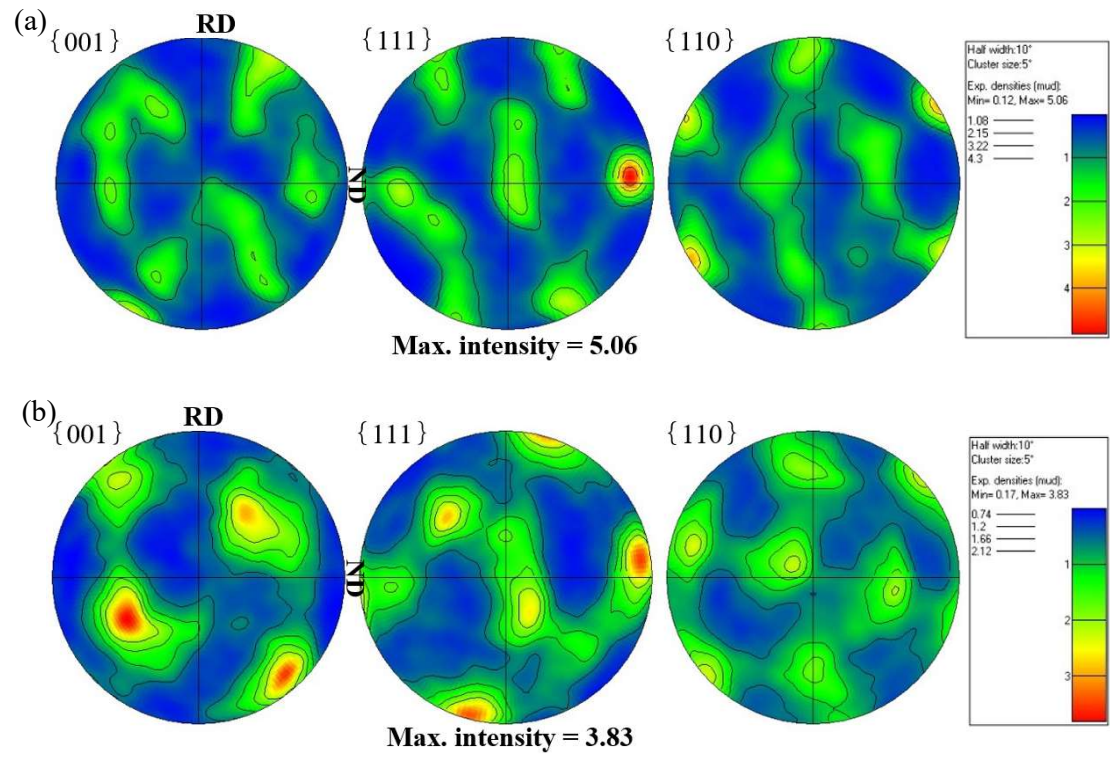


Fig. 5. Local Misorientation: (a) transition zone; (b) SPD zone; (c) data distribution.

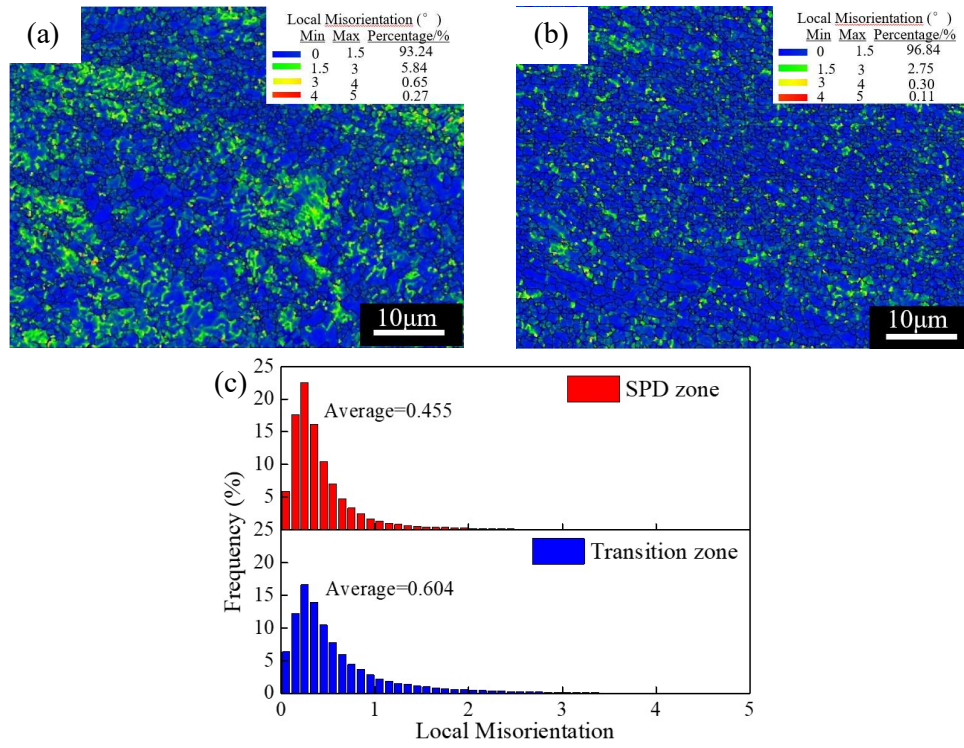


Fig. 6. TEM images of CL60 wheel steel after the rolling-sliding experiment: (a-c) SPD zone, at a depth around 40 μm below the surface; (d-f) transition zone, with a distance of 110 μm from the surface; (g-i) matrix material taken from the un-deformed region, i.e., 1 mm below the surface.

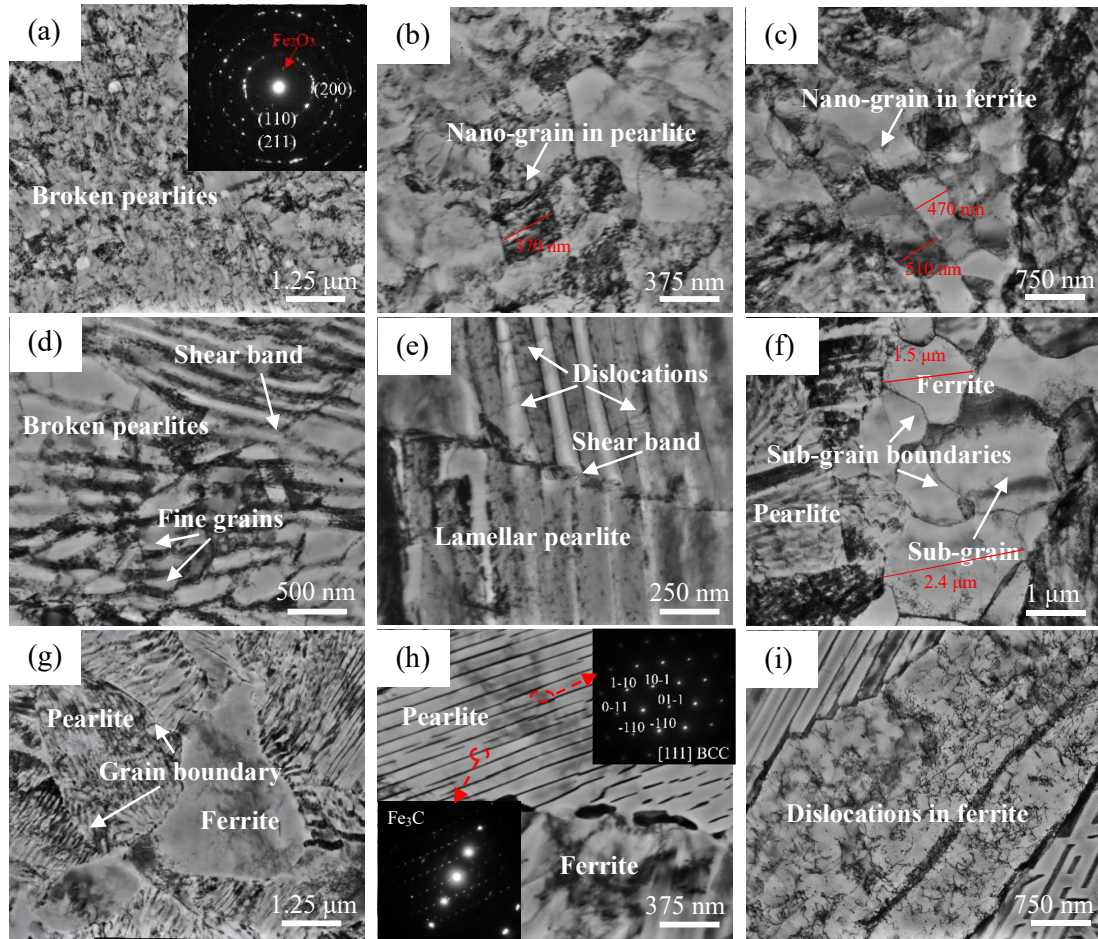


Fig. 7. XRD patterns in the SPD zone and the matrix material of CL60 wheel steel.

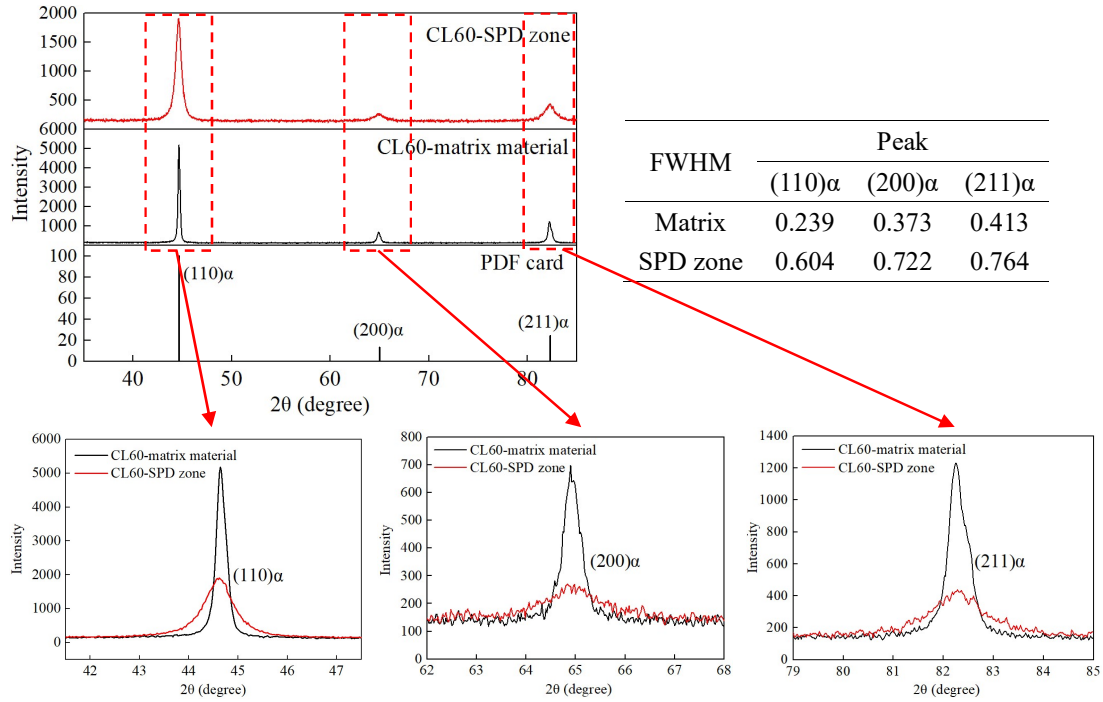


Fig. 8. SEM images of ER7 and C-class wheel steels after the rolling-sliding experiment: (a) SPD zone and (b) transition zone of ER7 wheel; (c) SPD zone and (d) transition zone of C-class wheel. The SPD zones and the transition zones were taken at the topmost region and 110 μm below the surface, respectively.

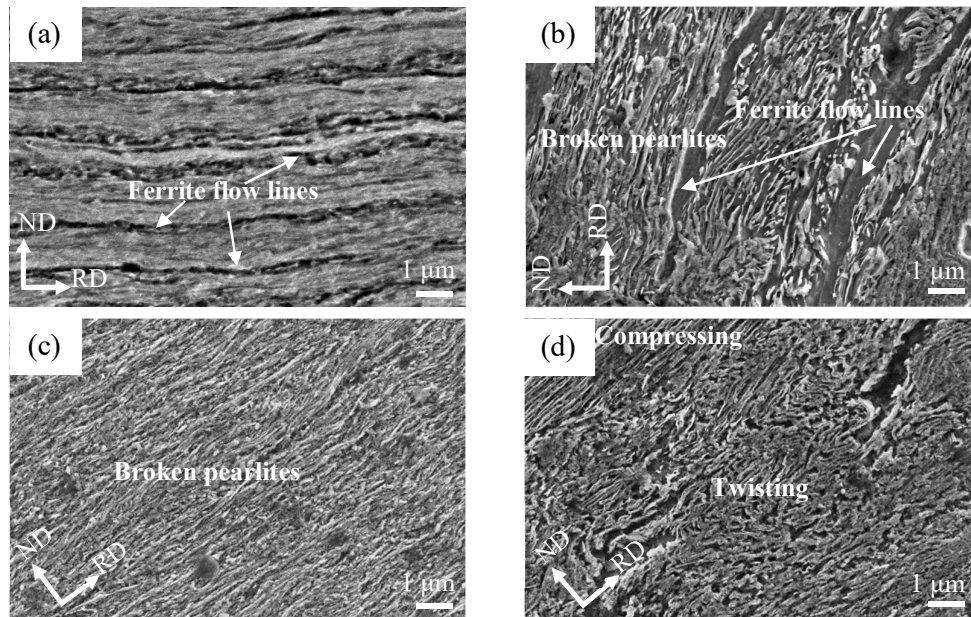


Fig. 9. TEM images of ER7 wheel steel in SPD zone (40 μm below the surface) after the rolling-sliding experiment.

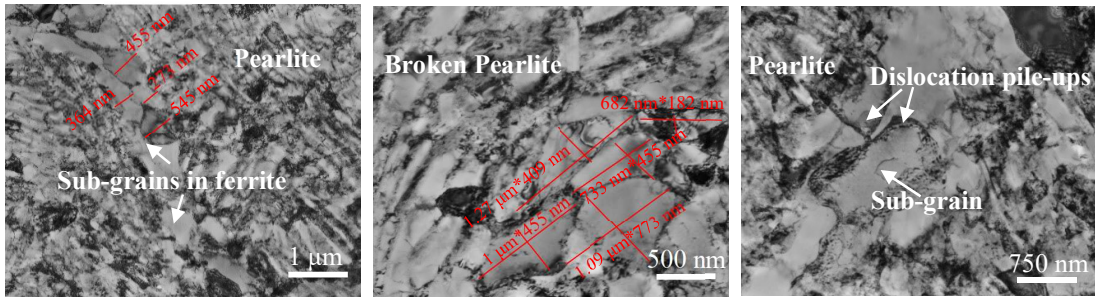


Fig. 10. TEM images of C-class wheel steel after the rolling-sliding experiment, (a-c) SPD zone, at a depth around 40 μm from the surface; (d-f) transition zone, at the depth of 110 μm from the surface; (g-i) matrix material taken from the un-deformed region at 1mm from the surface.

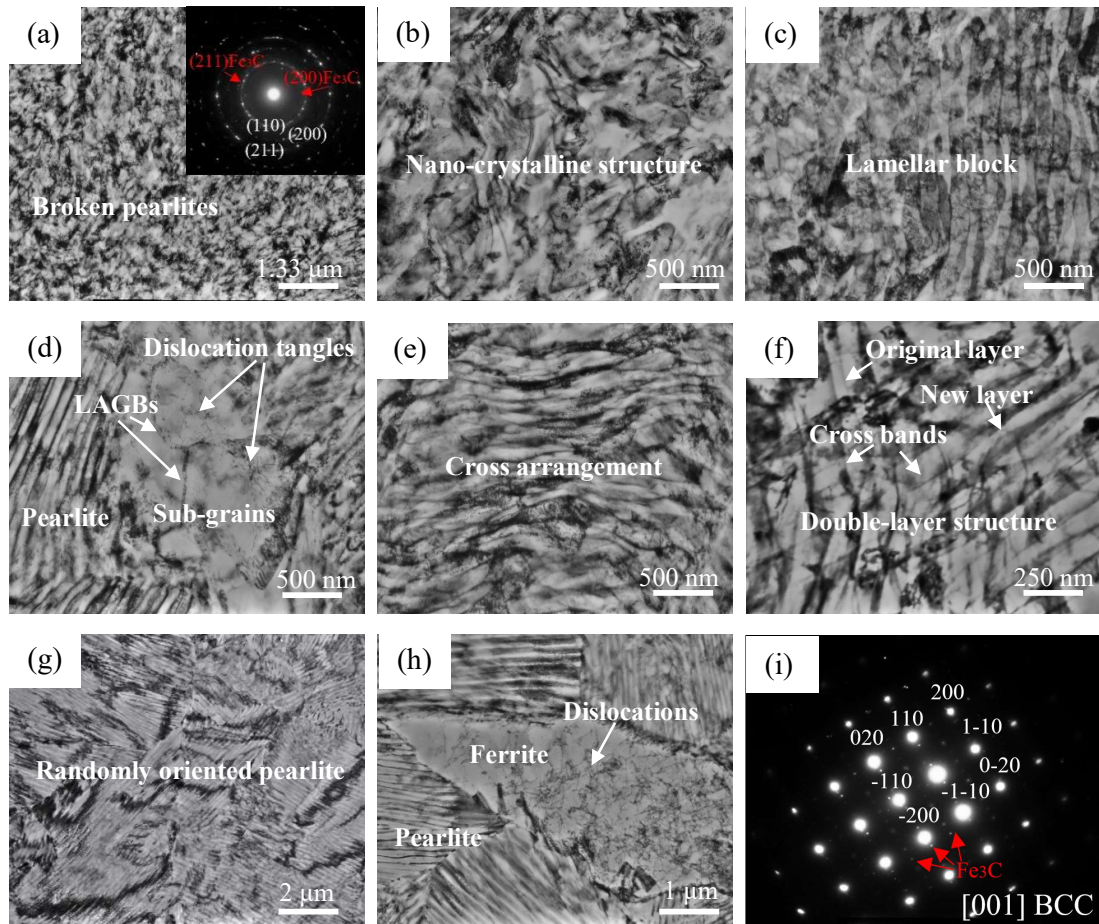


Fig. 11. Schematic illustration of cDRX and work-hardening: (a) process of cDRX [20]; (b) plastic deformation; (c) work-hardening; (d) mechanical analysis [22], where τ_{xz} is shear stress, k_0 is shear yield strength of the matrix material, k_t is shear yield strength of the transition zone material, k_s is shear yield strength of the SPD zone material.

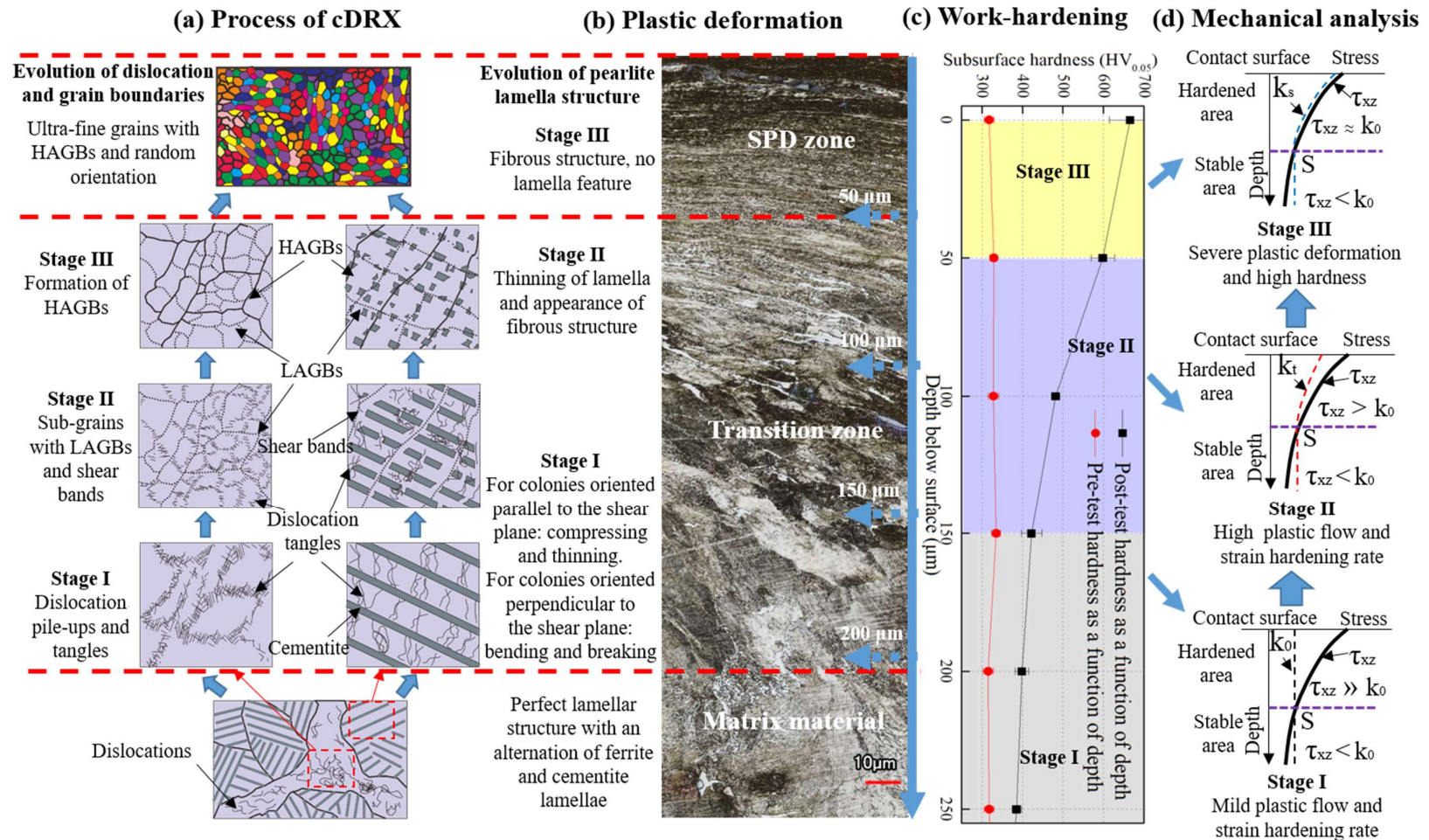


Fig. 12. (a) Mechanical analysis [22], where k_{ER7} , k_{CL60} and $k_{C-class}$ mean material shear yield strengths of ER7, CL60 and C-class steels; (b) sub-surface hardness variation with depth from surface.

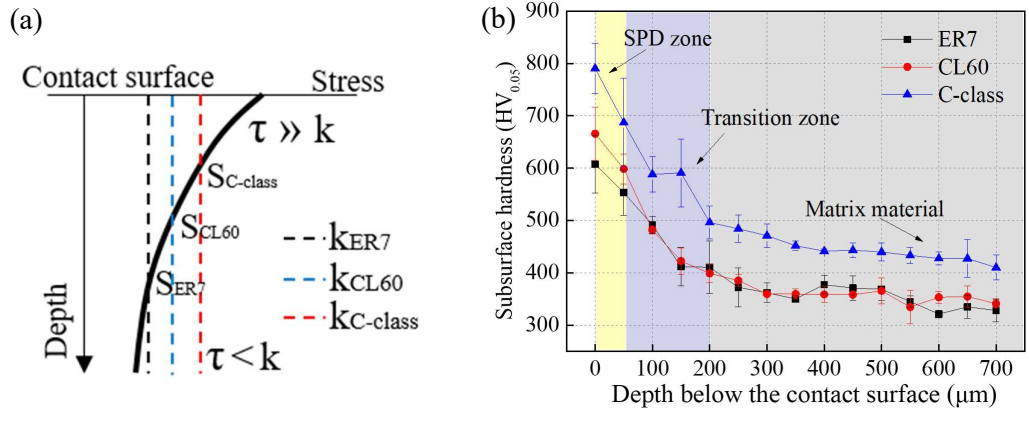


Fig. 13. Surface damages of (a) ER7 and (b) C-class wheels, and RCF cracks of (c) ER7 and (d) C-class wheels.

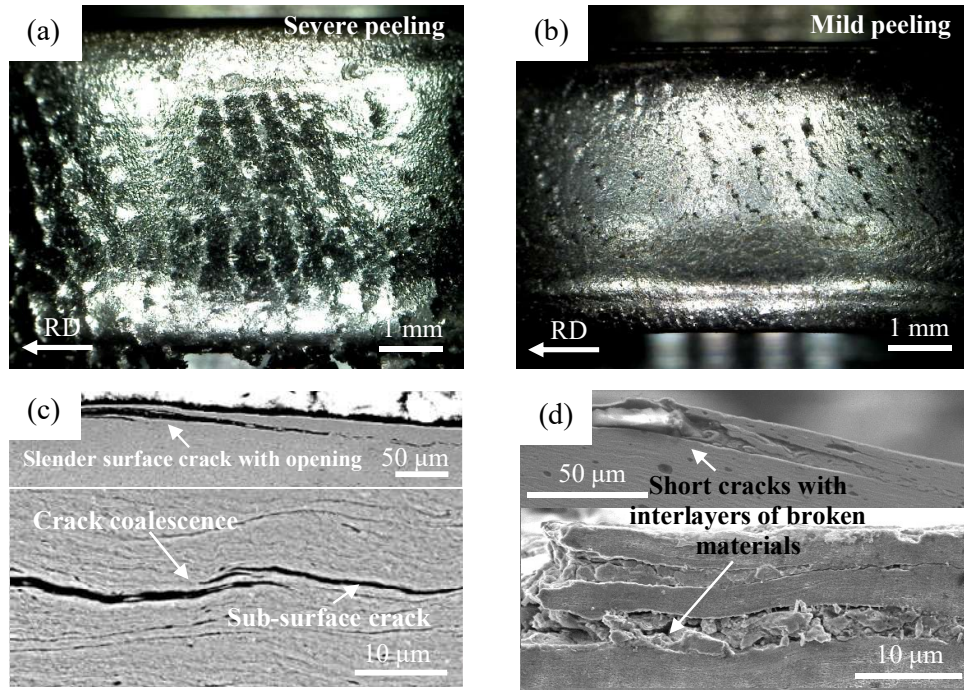


Table Caption

Table 1: Chemical compositions and hardness of wheel and rail materials.

Table 2: Comparison of microstructures and wear properties of three pearlitic wheel steels.

Table 1: Chemical compositions and hardness of wheel and rail materials.

Component	Grade	Chemical composition (wt%)					Hardness/HV _{0.5}
		C	Si	Mn	P	S	
Wheel	ER7	≤0.48	≤0.40	≤0.75	0.020	0.015	296±6
	CL60	0.55-0.65	0.17-0.37	0.50-0.80	0.035	0.040	327±11
	C-class	0.67-0.77	0.15-1.00	0.60-0.90	0.030	0.005-0.040	388±9
Rail	U75V	0.65-0.75	0.15-0.58	0.70-1.20	≤0.025	≤0.025	319±15

Table 2: Comparison of microstructures and wear properties of three pearlitic wheel steels.

Wheel grades	Matrix material			SPD zone (40 μm from surface)		Wear rate [6]/ $\mu\text{g}/\text{m}$	Average crack length [6]/ μm
	C/wt%	Ferrite	S_p/nm	Cementite lamellar structure	Grain structure		
ER7	≤ 0.48	Most	126.1 \pm 32	Fibrous structure, ferrite flow lines and broken pearlites	Non-equiaxed sub-grains of about 1 μm length, LAGBs	95	333 \pm 98
CL60	0.55~0.65	More	104.7 \pm 21	Fibrous structure, ferrite flow lines and broken pearlites	Equiaxed ultra-fine grains of about 400 nm diameter, HAGBs	61	207 \pm 101
C-class	0.67~0.77	Least	96.8 \pm 28	Fibrous structure, broken pearlites	Nano-crystalline structure, hardly measure the size of individual grain, HAGBs	24	71 \pm 32